









Experimental investigation of L- and H-mode detachment via the divertor Thomson scattering at ASDEX Upgrade

M. Cavedon^{1,2,*} , B. Kurzan², M. Bernert², D. Brida² , R. Dux², M. Griener² , S. Henderson³ , E. Huett^{2,4}, T. Nishizawa² , T. Lunt² , O. Pan² , U. Stroth^{2,4} , M. Wischmeier², E. Wolfrum² and the ASDEX Upgrade Team^{2,a}

¹ Dipartimento di Fisica ‘G. Occhialini’, Università di Milano-Bicocca, Milano, Italy

² Max Planck Institute for Plasma Physics, 85748 Garching, Germany

³ Culham Science Centre, Abingdon, OX14 3DB, United Kingdom of Great Britain and Northern Ireland

⁴ Physik-Department E28, Technische Universität München, James-Frank-Straße 1, 85748 Garching, Germany

E-mail: marco.cavedon@ipp.mpg.de

Received 8 November 2021, revised 24 February 2022

Accepted for publication 23 March 2022

Published 13 April 2022



CrossMark

Abstract

The capabilities of the newly installed divertor Thomson Scattering (DTS) diagnostic (Kurzan *et al* 2021 *J. Inst.* **16** C09012) at ASDEX Upgrade (AUG) have been demonstrated by measuring 2D electron densities n_e and temperatures T_e from attached to fully detached divertor conditions in L- and H-mode. The collected dataset is a breakthrough for divertor studies at AUG in which such measurements have been so far missing. Besides highlighting the strengths and limits of the DTS system, this work provides confirmations and new insights into detachment physics. The transition between partial and pronounced detachment correlates with a 2D redistribution of the electron density from the inner to the outer divertor in both L- and H-mode. In pronounced detachment, a strong parallel pressure gradient could be confirmed throughout the complete SOL. Finally, measurements of n_e and T_e of a stable X-point radiator revealed local temperatures as low as 1 eV within the confined plasma, whereas the pressure is shown to be constant on closed field lines.

Keywords: divertor, detachment, divertor Thomson scattering, L-mode, H-mode

(Some figures may appear in colour only in the online journal)

1. Introduction

A reliable solution for the power exhaust problem is one of the most critical challenges for realization of a fusion power

* Author to whom any correspondence should be addressed.

^a See Meyer *et al* 2019 (<https://doi.org/10.1088/1741-4326/ab18b8>) for the ASDEX Upgrade Team.



Original content from this work may be used under the terms of the [Creative Commons Attribution 4.0 licence](https://creativecommons.org/licenses/by/4.0/). Any further distribution of this work must maintain attribution to the author(s) and the title of the work, journal citation and DOI.

plant. Already for ITER, steady-state power handling requires 60 to 70% of the heat exhaust to be radiated throughout the divertor and the scrape-off layer (SOL) before intercepting the plasma-facing components (PFCs) [2]. DEMO will have to satisfy even more demanding conditions due to the larger power entering the SOL [3]. High dissipative divertor and SOL conditions, up to 90% of radiation, are now routinely obtained in several tokamaks [4–7] and labeled as ‘detached’. A detached divertor is associated with large pressure gradients along the SOL and connected to temperature as low as few eV in front

of the PFCs. The interplay and the relative importance of these processes as a function of the plasma parameters and divertor geometry is one of the key open questions in detachment physics. Recent experimental results on detachment can be found in [8], while theoretical works are reviewed in [9, 10].

The intrinsic 2D geometry and the large gradients of diverted plasmas make their experimental characterization extremely challenging. Among all the plasma parameters the electron density n_e and temperature T_e are of primary importance for diagnostics since measuring those allows to estimate the role of different underlying physical process. For this reason, at ASDEX Upgrade (AUG), a divertor Thomson scattering (DTS) system has been recently installed [1]. Thomson scattering provides non-perturbative local measurements of both n_e and T_e offering a unique insight into the divertor physics [11]. The AUG DTS system includes 26 channels extending from the inner (ID) to the outer divertor (OD) going through the X-point. It is furnished with a four-channel filter set to measure T_e from ≈ 1 eV to 50 eV and n_e from $1 \times 10^{19} \text{ m}^{-3}$ to $1 \times 10^{21} \text{ m}^{-3}$.

In this work, dedicated experiments have been carried out to characterize, for the first time at AUG, the behavior of n_e and T_e via DTS in the evolution from attached to detached divertor plasmas in both L- (section 2) and H-mode (section 3). A vertical plasma sweeping technique, similar to the one used in [12, 13], has been exploited to measure almost the complete divertor volume. L- and H-mode reveal similar qualitative behavior showing, however, differences in the local plasma parameter, for example in the private flux region (PFR). Subsequent experiments have been dedicated to the study of the X-point radiator (XPR) [14] and its impact on the pressure conservation on closed flux surfaces (FSs) (section 4). Finally, the conclusions and the outlook are given in section 5.

2. L-mode detachment

2.1. Experimental scenario (1D measurements)

The L-mode detachment discharges are a slight modification of the experiments performed in [15]: ohmic discharges with step-wise increasing line-averaged core density $n_{e,\text{core}}$ from $2 \times 10^{19} \text{ m}^{-3}$ to $5 \times 10^{19} \text{ m}^{-3}$ at a constant plasma current of 0.8 MA and toroidal magnetic field of 3.0 T. Figure 1 shows the reference discharge using a fixed plasma shape, i.e. the red one ($t = 2.0$ s) in figure 2. In this configuration, the DTS channels (in blue, figure 2) cross the whole divertor volume passing through the X-point. The geometry and the resolution, i.e. the extension of the scattering volume, of the DTS diagnostic is shown in figure 2. Note that the determination of the X-point position has uncertainty which could be up to few cm [16]. Figure 1(a) shows in blue the four steps in $n_{e,\text{core}}$ (delimited by the green vertical lines) as measured by the interferometer channel H-1 (see figure 2(b)), and in red the evolution of T_{div} , a figure of merit of the detachment state [17]. T_{div} approaches 0 eV towards the end of the discharges indicating complete detachment while the two spikes within every density phase, are due to beam blips for charge exchange measurements. Figures 1(b)–(d) shows respectively T_e , n_e ,

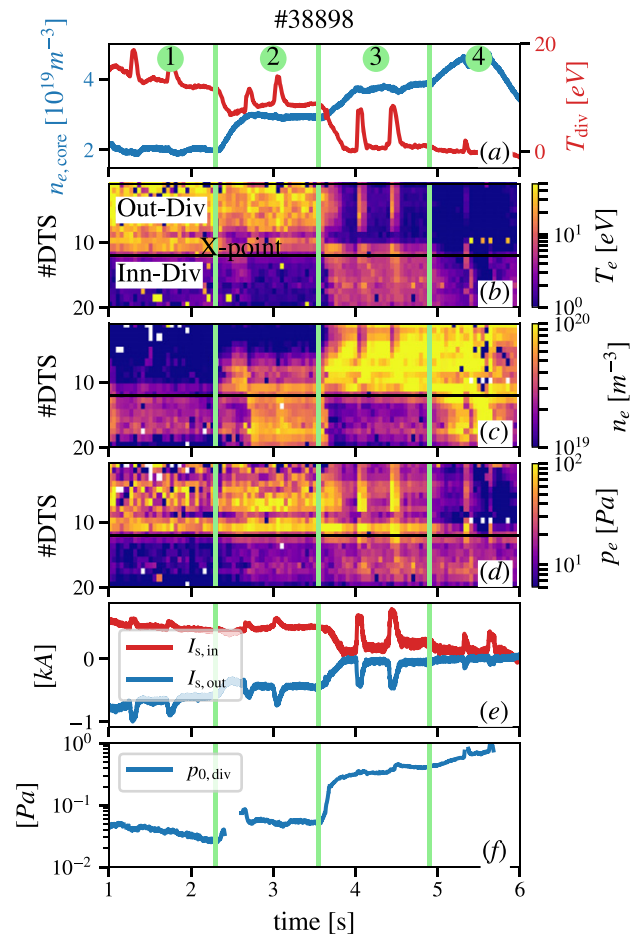


Figure 1. L-mode detachment reference discharge: (a) line-averaged core electron density $n_{e,\text{core}}$ in blue and the divertor temperature (a figure of merit of detachment) in red, (b)–(d) T_e , n_e and the resulting p_e from DTS, (e) divertor shunt current I_s at the inner (red) and outer (blue) divertor, (f) neutral pressure measured below the divertor dome.

and the resulting static p_e from DTS starting from channel #1 (inner-divertor (ID)) to channel #20 (outer-divertor (OD)). Channels from #20 to #26, which show similar results on the high-fields SOL, are excluded from the figure to focus on the ID and OD interplay. The X-point is located around channel #12, indicated by a horizontal black line. In this manuscript, the electron pressure calculated from the DTS is always the static pressure, i.e. $p_e = n_e T_e$. Figure 1(e) illustrates the evolution of the divertor shunt currents at the ID $I_{s,\text{in}}$ (red) and the OD $I_{s,\text{out}}$ (blue) while figure 1(f) shows the neutral pressure measure below the divertor dome.

The diverted plasma starts from well-attached condition (step 1) with very high T_e (figure 1(b)) and low n_e (figure 1(c)) at the OD and moves towards high-recycling conditions (step 2) at the second $n_{e,\text{core}}$ step. This phase is labeled as detachment onset in [15] and shows a clear high field side high-density front (HFSHDF) at the ID (figure 1(c)) [18]. A relatively minor increase of the core density at $t = 3.6$ s triggers a rapid transition to a detached divertor. The electron temperature at the OD drops from a few tens of eV to less than 2–3 eV. The reduction of T_e is accompanied by an increase of n_e of roughly one order of magnitude at the OD. Note that

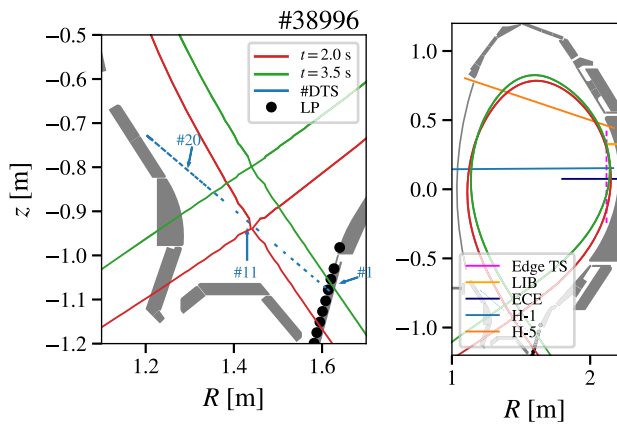


Figure 2. Plasma shape scan to obtain 2D DTS measurements. The reference shape is shown in red while in green the other extreme of the shape scan. The figures shows also the position of the different diagnostic used in this work.

the drop in T_e is faster than the duration of density ramp which highlights the nature of a step-like transition of the detachment process. The electron pressure drops at the OD (figure 1(d)) and its conservations along the SOL field lines will be investigated in section 2.2. The ID reacts the other way around: the HFSHDF vanishes and T_e increases. However, the DTS measurements at the ID are performed further upstream compared to the one at the inner-divertor. More detailed analysis of the ID will be shown in section 2.2 where the plasma is swept vertically. In the same way, the divertor shunt currents in figure 1(d) drop in the transition from step 2 to step 3 with $I_{s,out}$ consistently decreasing first. This observation might offer a good test for any causality model of detachment. The neutral pressure measured below the divertor dome is observed to consistently increase by almost an order of magnitude. Finally, step 4 leads to even colder OD temperatures ($T_e \lesssim 1$ eV) while the inner one starts to cool down again.

This step-like behavior of the OD at the detachment transition has been already observed at DIII-D [13], however only in H-mode. The transition has been previously explained via a bifurcation in the $\mathbf{E} \times \mathbf{B}$ -drift [19]. Dedicated modelling would be required to confirm such claim which is beyond the scope of this work. The possibility of a bifurcation solution of the divertor plasma state has been also demonstrated in [20]. The L-mode discharges performed in this work do not show any ‘fluctuating state’ before detachment as observed in [15]. X-point fluctuations are only visible during the beam blips within step 3 showing that the divertor input power is a condition for this type of instability.

2.2. 2D n_e and T_e maps towards detachment

A vertical (z -) sweep of the X-point has been employed to collect n_e and T_e of a large portion of the divertor volume. During the scan the magnetic topology of the divertor plasma has been preserved. To avoid a double null configuration, the upper plasma shape has been kept as constant as possible effectively reducing the plasma volume. The two extreme plasma shapes used during the sweeps are shown in figure 2. The complete z -scan height lasts ≈ 2 s and has been applied to all four

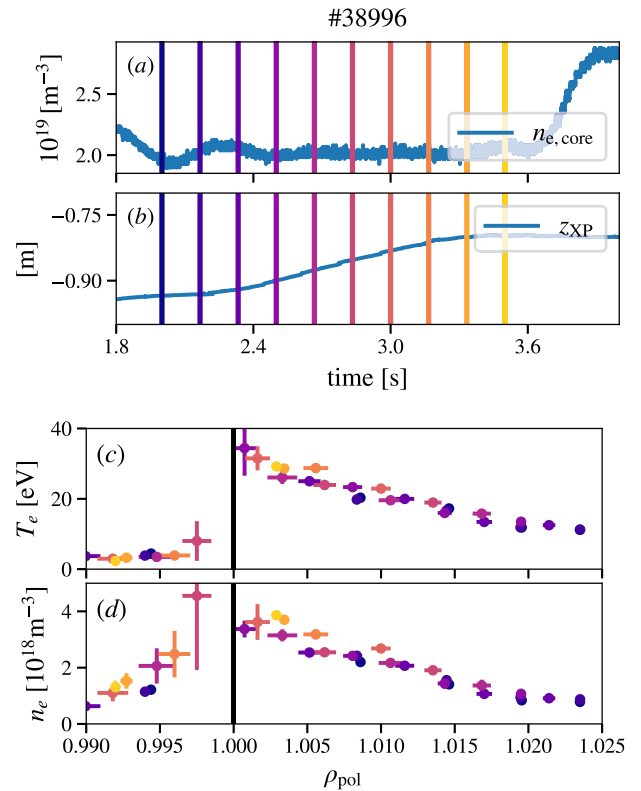


Figure 3. Consistency check of the diverted plasma conditions during a X-point sweep: (a) line-averaged electron density, (b) z -position of the X-point, (c) T_e and (d) n_e from the outer target LP. The vertical lines in (a) and (b) indicates the time points (averaged over 50 ms) shown in (c) and (d).

phases shown in figure 1 in two different discharges. Note that a z -sweep is ideal, given the DTS geometry, to provide measurements along FSs. Figure 2 reports the position of the different diagnostics used in this work: the DTS diagnostics is shown in blue. The extension of the marker along the laser corresponds to the size of the scattering volume and hence of the DTS radial resolution (more details in [1]). The same applies to the mid-plane edge TS, illustrated in magenta. Furthermore, in this work, the integrated data analysis framework IDA [21] has been used to obtain n_e and T_e profiles which, at the edge, are mostly constrained by the ECE (blue), the lithium beam (LIB in orange) and the edge TS. Finally, in black, the position of OD Langmuir probes (LP) is reported.

The consistency of the diverted plasma condition during the whole scan has been controlled using the LP. Figure 3 compares the outer target measurements of n_e and T_e during an X-point sweep in attached conditions. Figures 3(a) and (b) show respectively $n_{e,core}$ and the X-point height during such a scan. The vertical lines indicate the different time-points selected to check the consistency of the n_e (figure 3(c)) and T_e (figure 3(c)) target profiles from the LPs. The profiles well overlap indicating that the target profiles are constant during the entire scan, as well as the mid-plane profiles. This does not assure the consistency of the plasma parameters in the whole divertor volume, but it is a zero-order test that the diverted plasma is not changing dramatically. Tackling this problem experimentally is however not possible since localized 2D measurements of

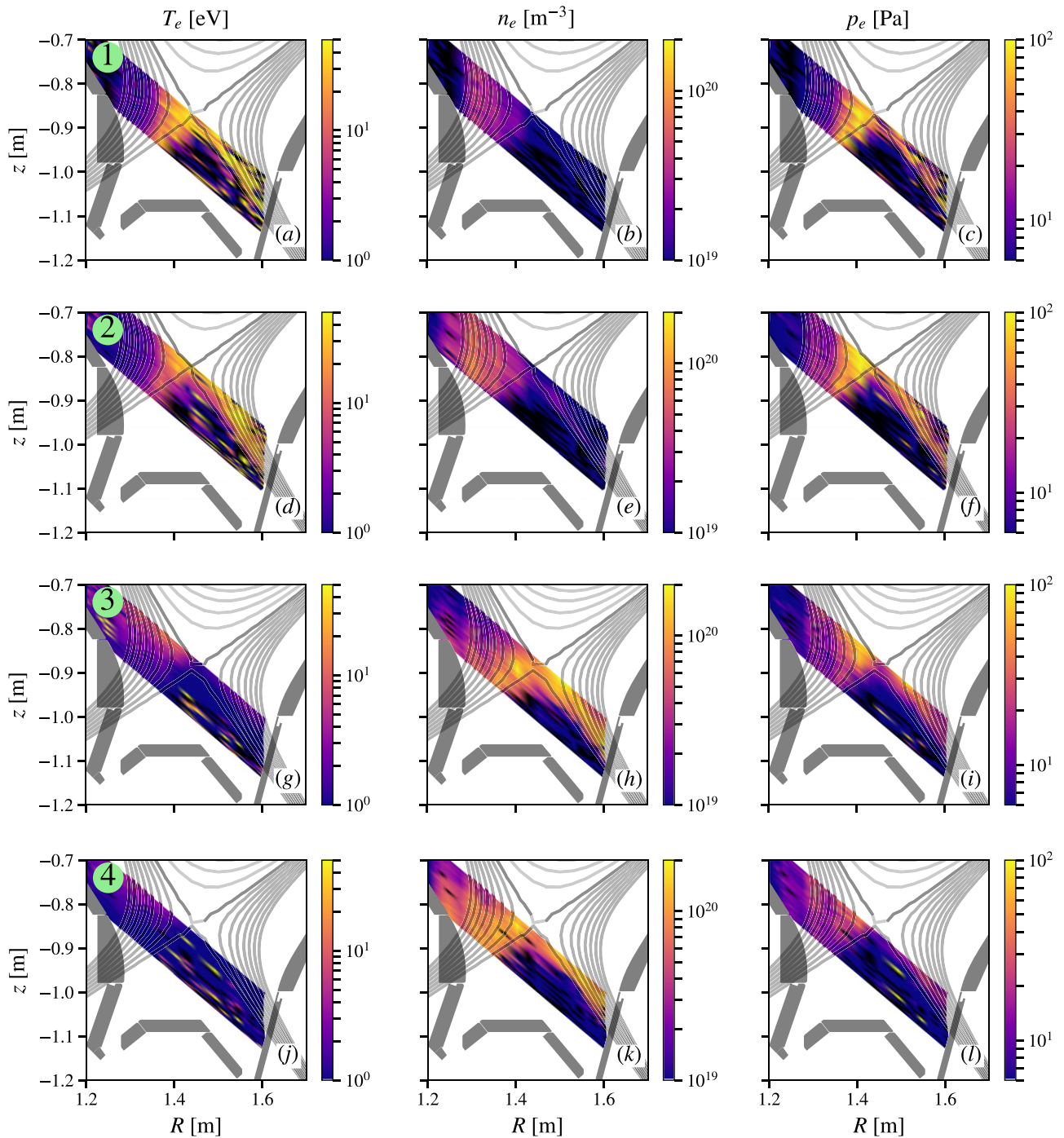


Figure 4. Two-dimensional measurements with the DTS in L-mode of T_e (left column), n_e (middle column), and the resulting static p_e (right column) at increasing $n_{e,\text{core}}$ (from top to bottom).

any divertor plasma parameters are not available at this stage. Furthermore, the consistency of the target profiles could be only checked in attached and high recycling conditions, i.e. steps 1 and 2 (not shown), while detached plasmas could not be investigated due to the absence of target data. The upcoming thermal divertor helium beam will provide 2D n_e and T_e in the OD allowing a direct proof of the consistency of the diverted plasma conditions during such scans.

Figure 4 shows the resulting 2D measurements for T_e (left-hand column), n_e (central column), and the calculated electron pressure p_e (right-hand column) from DTS, starting from

step 1 (first row), i.e. $n_{e,\text{core}} = 2 \times 10^{19} \text{ m}^{-3}$, to step 4 (last row), $n_{e,\text{core}} = 5 \times 10^{19} \text{ m}^{-3}$. The combination of the z -sweep and the large number of channels of the DTS permits detailed measurements along the FSs. Note that the color bar range in figure 4 for n_e , T_e , and p_e are kept constant for all the density steps to highlight the relative changes.

Step 1 (figures 4(a)–(c)) is characterized by low densities and high temperatures at the OD, which coincides with a low signal-to-noise ratio and hence large scattering for the DTS. At the ID, a slight HFSHDF is already present. Figure 5 compares the mid-plane pressure measured by Thomson scattering

(TS, in green) and IDA (integrated data analysis of TS, ECE and lithium-beam, in red) [21] with DTS (in blue and in navy the flux-surfaces average) and the LP (in black) at the OD for the four different density steps (figures 5(a)–(d)). During step 1 (figure 5(a)), the electron pressure is constant on field lines in the SOL indicating that the OD divertor is attached. The increase of $n_{e,\text{core}}$ in step 2 leads to electron densities of about 10^{20} m^{-3} in the HFSHDF (figure 4(d)) together with a slight reduction of T_e at both the ID and OD while the overall distribution of the electron plasma parameters remains similar. The pressure on the SOL FSs is mostly constant, except next to the separatrix where a reduction of p_e is observed (figure 4(b)), similar to what is observed in [15]. These conditions are often labeled as partial detachment [23]. A drastic change in the 2D distribution of n_e and T_e is measured after the transition to detachment, i.e. in step 3 (figures 4(g)–(i)). A large increase of n_e , up to $\approx 10^{20} \text{ m}^{-3}$, at OD coincides with the disappearance of the HFSHDF. Such behavior is indicative of the interplay between OD and ID, most likely mediated by the $E \times B$ drift, and recalls the phenomena of the divertor oscillations [24, 25]. The electron temperature drops to a few eV close to both the inner and the outer target (figure 4(g)) and results in a poloidal electron pressure gradient (figure 4(i)). When comparing the mid-plane to the divertor pressure (figure 5(c)), a reduction of more than an order of magnitude is observed within the DTS measurement volume, in particular, next to the separatrix. This can be better seen when plotting p_e as a function of z at fixed ρ_{pol} location (figure 6). The LPs have been excluded from the comparison since their interpretation becomes unreliable at low temperatures. In particular, both the sweep LP and the triple probes return larger T_e values compared to the DTS as already previously observed [26] and explained by a non-Maxwellian electron distribution [27]. Other drawbacks of LP measurements at low T_e are the fact that the resistance in the bulk plasma is no longer negligible compared to the sheath resistance [28] while also the presence of resistances in the cables and in the measurement system leads to an overestimation of T_e [29].

Note that in figures 5(a) and (b) the DTS measurement results at a fixed ρ_{pol} have been averaged, while in figures 5(c) and (d) they were not because of the evident poloidal gradient. A further reduction of T_e , as measured with the DTS, is obtained when increasing $n_{e,\text{core}}$ to $5 \times 10^{19} \text{ m}^{-3}$ (figure 4(j)). However, the minimum pressure measured by the DTS remains constant compare to step 3 (figures 5(c) and (d)) while it is the mid-plane p_e that decreases. A similar degradation of the plasma core confinement when going to pronounced detachment has been also observed previously [30–32].

3. H-mode detachment

To characterize the H-mode detachment via DTS, a series of discharges has been performed with T_{div} ranging between 15 eV and 1 eV at constant heating power of about 10 MW, plasma current ($I_p = 0.8 \text{ MA}$), and field ($B_t = -2.5 \text{ T}$) while changing only the nitrogen fuelling. Within every discharge, a constant phase of about 2.5 s has been programmed to allow for the same z -scan of the X-point as performed in

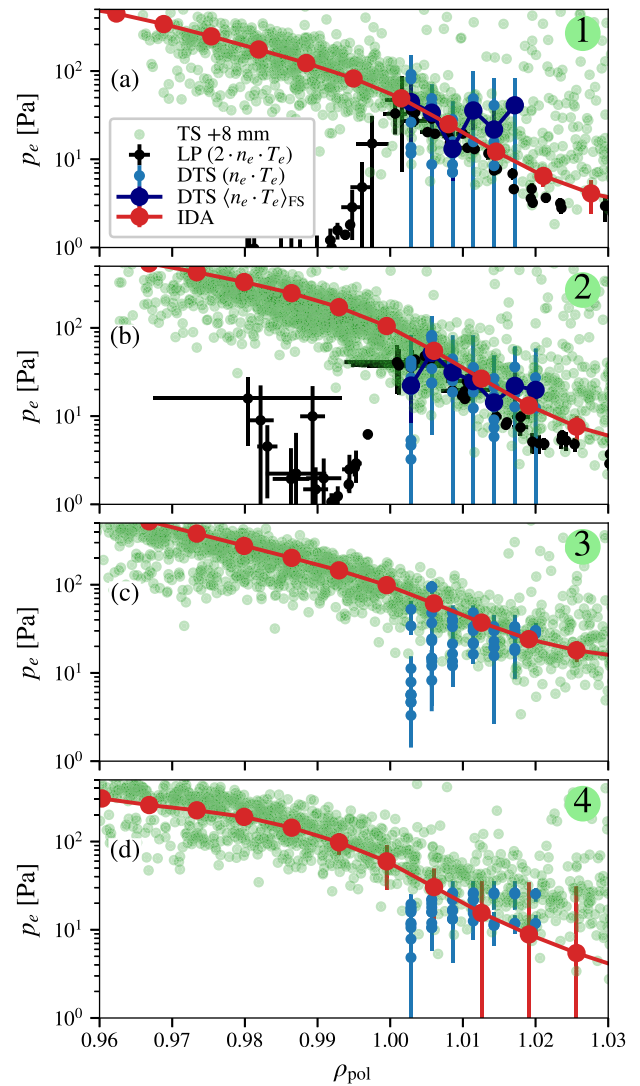


Figure 5. Comparison between the mid-plane electron pressure (TS in green and IDA in red) to the DTS (blue for the single data points and navy for the flux-surface average in figures (a) and (b)) and LP (black) measurements at increasing $n_{e,\text{core}}$ (top to bottom). The TS profiles has been shifted outward by 8 mm as routinely done at AUG [22] while the factor 2 on the LP p_e is to account for the dynamic pressure.

L-mode (figure 2). Figure 7 shows the overview of a typical H-mode discharge used in this study: (a) ECRH (blue) and NBI (red) external heating power at a fixed plasma current (black), (b) edge (red) and core (black) line averaged densities (measured respectively with the interferometer channels H-5 and H-1, figure 2(b)), (c) nitrogen (red) and deuterium (black) fuelling, (d) T_{div} , (e) X-point height, and (f) ELM frequency. The discharge is divided in two phases, i.e. before and after 5 s, with different N_2 seeding rates in order to obtain two different values of T_{div} . Within each phase, a z -scan of the X-point is performed to obtain 2D DTS measurements. Figure 8 compares the outer target T_e and n_e ELM synchronized profiles as measured from the LP at different time points along a vertical plasma sweep. Within the large error bars, which are typical for ELMy H-modes, the profiles agree and therefore the same considerations as for the L-mode case might be also valid in

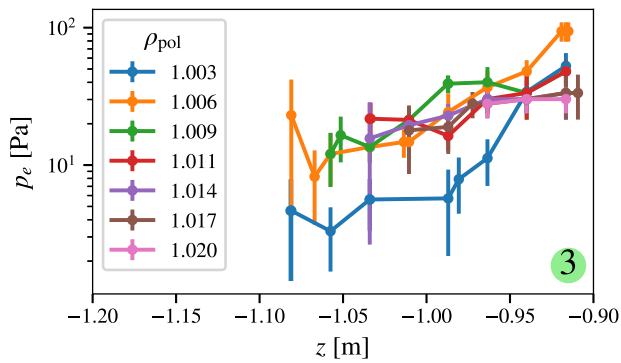


Figure 6. DTS electron pressure as function of z at several ρ_{pol} , i.e. on different FSs.

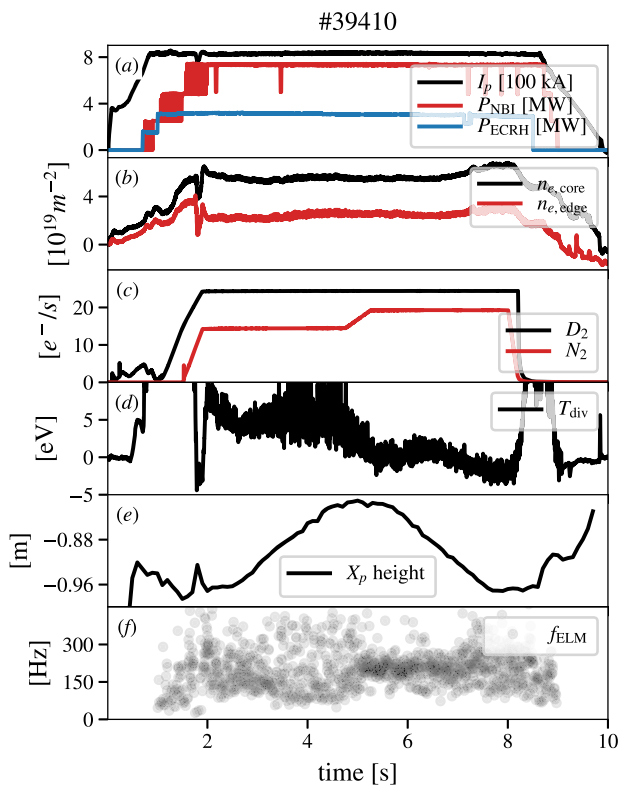


Figure 7. Reference discharges for the study of H-mode detachment via DTS: (a) plasma current (black), NBI (red) and ECRH (blue) external heating power; (b) edge (red) and core (black) line average electron density; (c) nitrogen (red) and deuterium (black) gas fuelling; (d) T_{div} ; (e) X-point z position; (f) ELM-frequency.

H-mode. However, since the error-bars reach up to 50%, this comparison is only a rough cross-check of large, i.e. of order of magnitude, systematic deviations when scanning the plasma vertically.

The analysis of the detachment in H-mode is much more challenging due to the presence of ELMs. When going to high deuterium gas puffing and nitrogen seeding, i.e. towards detachment, the ELMs get smaller and the frequency f_{ELM} increases rapidly above 150 Hz (figure 7(e)) and moves towards a continuous exhaust till a complete ELM-suppression is observed when the XPR is well within the confined region [33–35]. During this evolution, ELM filtering of the DTS data

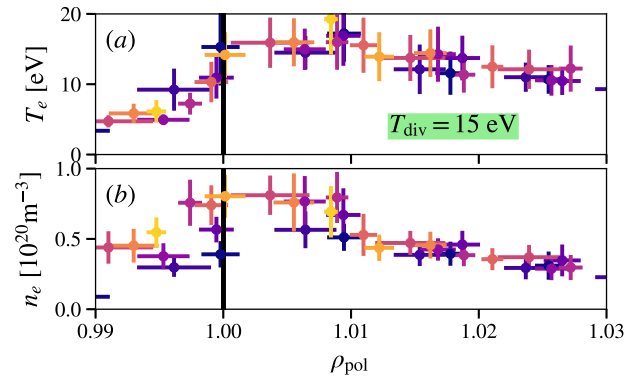


Figure 8. Outer target T_e (a) and n_e (b) profiles from the LP at different time points during an X-point scan in H-mode, attached conditions.

was not possible in detached conditions, i.e. $T_{\text{div}} < 4$ eV [32]. An alternative would be to use argon or krypton instead of nitrogen to keep f_{ELM} low. On the other hand, the low f_{ELM} makes the discharges more exposed to impurity accumulation and to have the most stable conditions for the X-point sweep, nitrogen is the best choice.

Figure 9 shows the 2D measurements of T_e (left column), n_e (central column), and the resulting p_e (right column) from attached ($T_{\text{div}} = 15$ eV, first row) to detached conditions ($T_{\text{div}} = 1$ eV, last row). As for the L-mode cases, in figure 10 the mid-plane p_e profiles from IDA (red) and TS (green) are compared to the DTS data (blue the single data points and in navy the flux-surface average) and the LP (black) at the outer target. Starting from attached conditions (figures 9(a)–(c)), a well-developed HFSHDF is present while, in the OD, the electron density is still relatively low, i.e. on the order of 10^{19} m^{-3} , resulting in high electron temperatures $T_e \approx 50$ eV. At these conditions, the electron pressure is conserved along the field lines in the SOL (figure 10(a)). As mentioned before, the large scatter in the TS and DTS data is a result of their limited laser repetition frequency and hence complexity in the ELM filtering.

An unexpected outcome of the 2D measurements in the attached H-mode is the high density n_e in the PFR (figure 9(b)) of around $1 \times 10^{20} \text{ m}^{-3}$ at about 10 cm below the X-point, whereas T_e is approximately 1 eV (figure 9(a)). In L-mode, the n_e in the PFR is below $1 \times 10^{19} \text{ m}^{-3}$, i.e. at the detection limit of the DTS (figure 4). A similar high density in the PFR is observed also in the DIII-D tokamak in forward field [36] and in the presence of the HFSHDF front but not always as extended as shown in this work [8]. However, given the low temperatures at the limit of the DTS range and the uncertainties in the X-point position, further investigations are necessary to exactly determine the size of the PFR high-density region. On the other hand, the fact that the resulting pressure (figure 9(c)) shows the expected drop close to the separatrix as well as the reduction of the high n_e at the lower end of the 2D measurements and just within the confined region, support the validity of the measurements. $E \times B$ -drifts and/or anomalous transport might be the reasons for such behavior which is an interesting case study for divertor modeling.

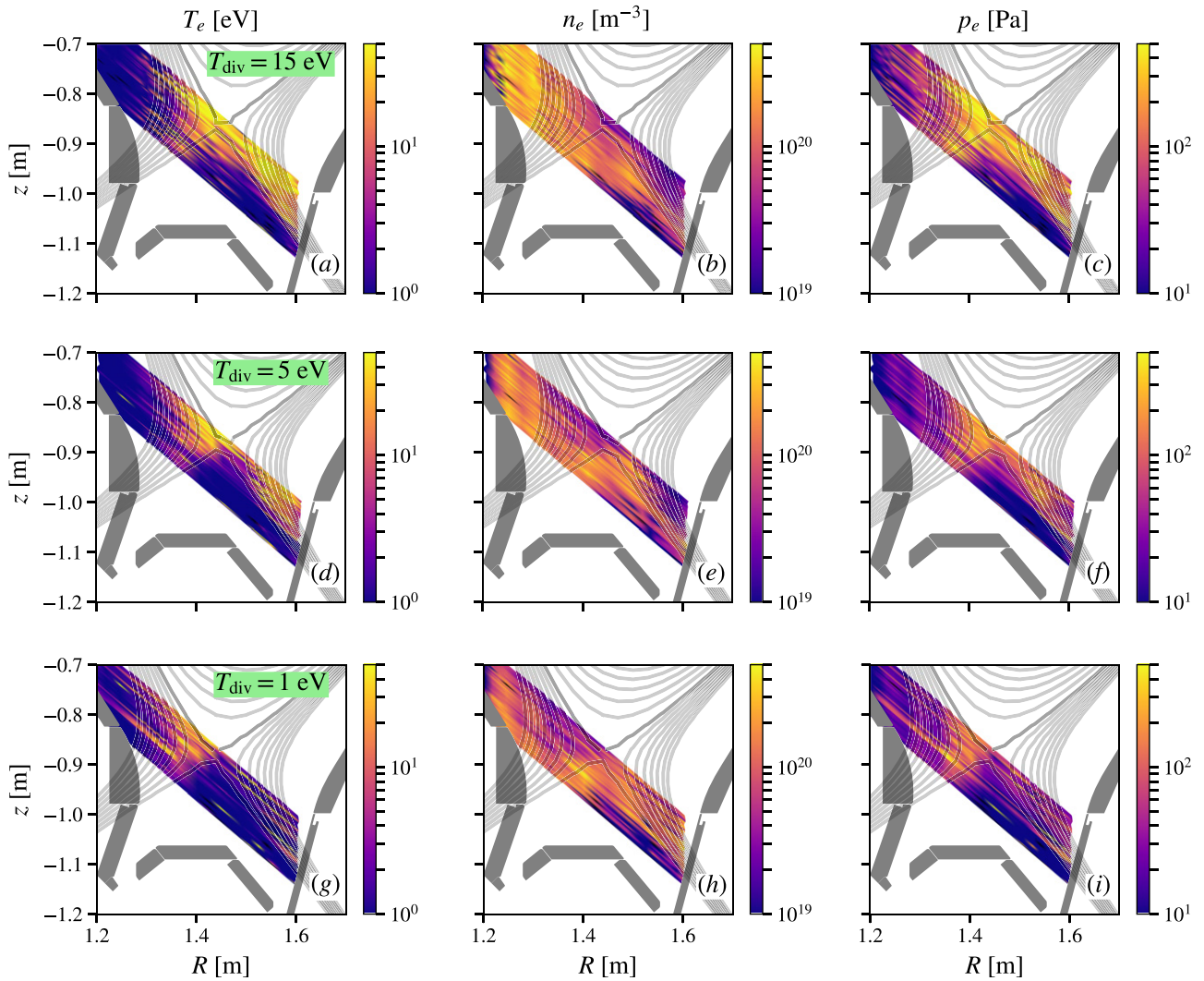


Figure 9. Two-dimensional measurements with the DTS in L-mode of T_e (left column), n_e (middle column), and the resulting p_e (right column) at decreasing T_{div} (from top to bottom).

Figures 9(d)–(f) show the electron density, temperature and pressure at $T_{\text{div}} = 5$ eV where, according to [32], the divertor is partially detached and close to complete detachment. The 2D distribution of the plasma parameters does not change substantially compared to the 15 eV case (figures 9(a)–(c)) but the increase of the nitrogen seeding leads to an overall reduction of T_e at both the ID and OD. When comparing the mid-plane to the divertor electron pressures, a parallel p_e gradient is observed between the mid-plane and the DTS data, while the LP data match remarkably well the mid-plane profile. As discussed before, a straight-forward explanation would be the overestimation of T_e by the LP but at temperatures of about 10 eV (figure 9(d)) the LP interpretation should be reliable. On the other hand, a certain pressure drop is expected when going to partial detachment. The upcoming thermal helium beam which is being installed in the OD of AUG will provide a further independent 2D measurement of p_e and will shed light in this discrepancy.

The further increase in the nitrogen seeding induces the complete detachment of the divertor plasma, i.e. T_{div} reaches

1 eV. The OD T_e drops to 1–3 eV (figure 9(g)) while the density increases to about $1 \times 10^{20} \text{ m}^{-3}$ (figure 9(h)). Furthermore, the electron pressure is about one order of magnitude lower compared to the mid-plane (figure 10(c)) demonstrating a strong dissipation along the SOL field lines. The transition from $T_{\text{div}} = 5$ eV to 1 eV induced by N seeding is similar, in terms of the relative change of the divertor plasma parameters, to the detachment transition in L-mode (figure 4). However, it is not clear from this work if such a transition happens abruptly, i.e. within a small variation of the main plasma parameters, as in the L-mode case and in the DIII-D tokamak [13]. Previous work at AUG has shown that the transition from partial to complete detachment happens gradually on both targets or where the heat flux and pressure were measured by the LP [32]. However, as stated before, the interpretation of the LP data might be misleading and therefore a detailed comparison is envisaged.

4. X-point radiator scenario

The development of real-time controls of the detachment evolution allowed the exploitation of high radiation scenarios in

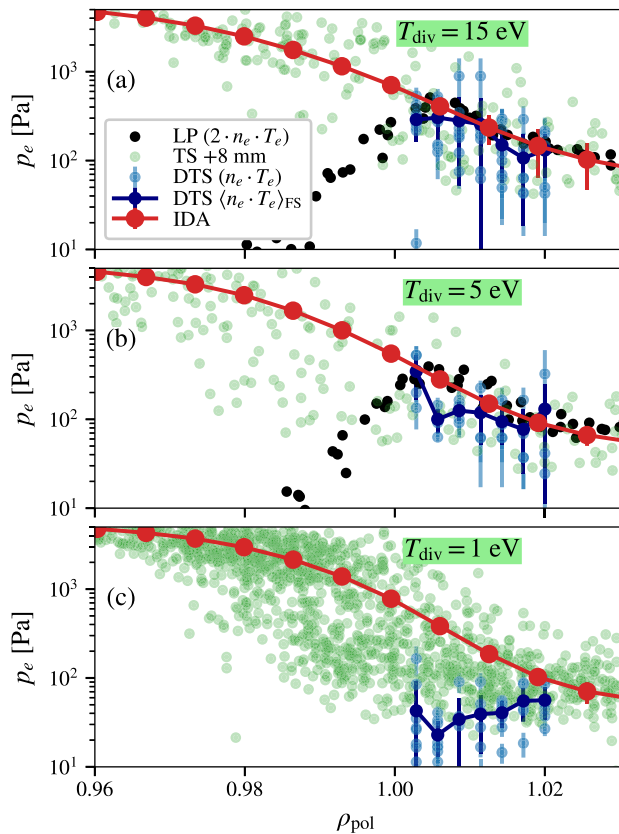


Figure 10. Comparison between the mid-plane electron pressure (TS in green and IDA in red) to the DTS (blue the single data points and in navy the flux-surface average) and LP (black) measurements at decreasing T_{div} in H-mode (top to bottom).

which an XPR radiates a power fraction of more than 75% of the input power within the confined region [14, 37–39]. In this area, a strong local reduction of T_e has been suggested by Balmer and NIII measurements [40] due to the large radiation while the electron density is shown to increase in order to keep the pressure constant on a closed flux surface. However, *a priori*, a parallel pressure gradient even on closed field lines cannot be excluded due to the extreme conditions at the XPR and the large flux expansion at the X-point. For the first time, the new DTS system at AUG permits the experimental investigation of the electron plasma parameters at the XPR, a crucial insight to understanding the physics behind it.

The comparison of the mid-plane profiles to the X-point measurements requires high accuracy in the relative alignment. Due to the large flux expansion close to the X-point, the DTS is very limited when trying to measure at $\rho_{\text{pol}} < 0.99$. Figure 11 shows the two equilibria used in this work. The configuration in figure 11(a) allows normal plasma operations without any limitation to the power arriving at the OD since the outer strike point is still on the OD target. On other hand, the DTS can only measure up to $\rho_{\text{pol}} = 0.997$ which corresponds, at the mid-plane, to only roughly 1.5 mm inside the separatrix. The most extreme case in which DTS can measure the furthest within the confined region, i.e. 5 mm inside the separatrix at the mid-plane, is shown in figure 11(b). In this case, however, only a detached plasma is allowed to be placed so close

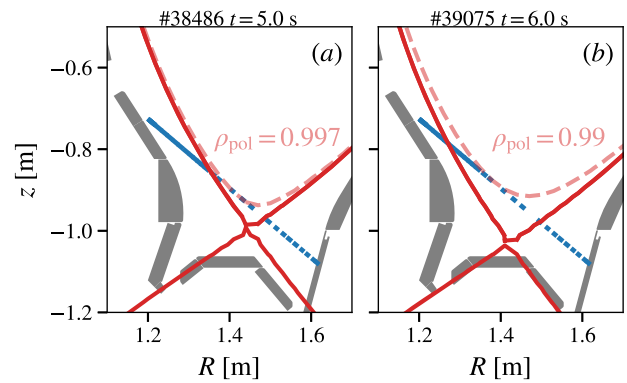


Figure 11. Comparison of the plasma shapes used to investigate the XPR electron plasma parameters.

to the divertor dome to protect the PFCs. Due to these limitations, two different strategies have been adopted to compare the mid-plane to the X-point pressure: (i) using the equilibrium in figure 11(a), the plasma has been driven from attached to the XPR regime making use of the attached phase to align the profiles, i.e. $p_e = \text{const}$ on a flux surface, and then looking at the time evolution; (ii) first induce an XPR and then shift the plasma to the configuration in figure 11(b) to obtain a 2D map of n_e and T_e within the confined region. Unfortunately, the second approach did not work because the plasma could not be kept stationary during the vertical shift onto the divertor dome. However, it offered an insight on the typical plasma parameters of the XPR (figure 12): electron temperatures of 3 to 5 eV (figure 12(a)) at densities of 1 to $3 \times 10^{20} \text{ m}^{-3}$ (figure 12(b)). It is interesting to notice that, in these conditions, the outer SOL is hotter but less dense than the XPR.

The equilibrium in figure 11(a) has been used in combination with a discharge with similar parameters as the one presented in [35]. Figure 13 shows an overview of the reference discharge: (a) ECRH (blue) and NBI (red) external heating power at a fixed plasma current (black), (b) edge (red) and core (black) line averaged densities, (c) nitrogen (red) and deuterium (black) fuelling, (d) T_{div} , (e) XPR penetration. As in [35], ELM suppression is observed when the XPR-height is larger than approximately 5 cm, hence from roughly 5 s to 7 s. The phase between 2.0 s and 3.5 s is used as a reference to relative align the mid-plane electron pressure profile. In figures 14(a) and (b) the electron temperature T_X and density n_X at the X-point are shown calculated by averaging the three DTS channels at roughly $\rho_{\text{pol}} = 0.997$ (see figure 11). A change in the electron plasma parameters near the X-point is observed starting at 4 s when the XPR reaches the DTS channels, i.e. roughly 5 cm above the X-point. The movement of the XPR to 10 cm above the X-point induces a rapid drop of T_X to approximately 1 eV and an increase of n_X to $2 \times 10^{20} \text{ m}^{-3}$. The achievement of such plasma conditions within the confined region without losing the discharge or even deteriorating the confinement too strongly highlights the effectiveness of the detachment control methods in nowadays devices. The mid-plane density and temperature profiles are shown in figures 14(c) and (d) where different colors indicate different positions. While the density remains more or

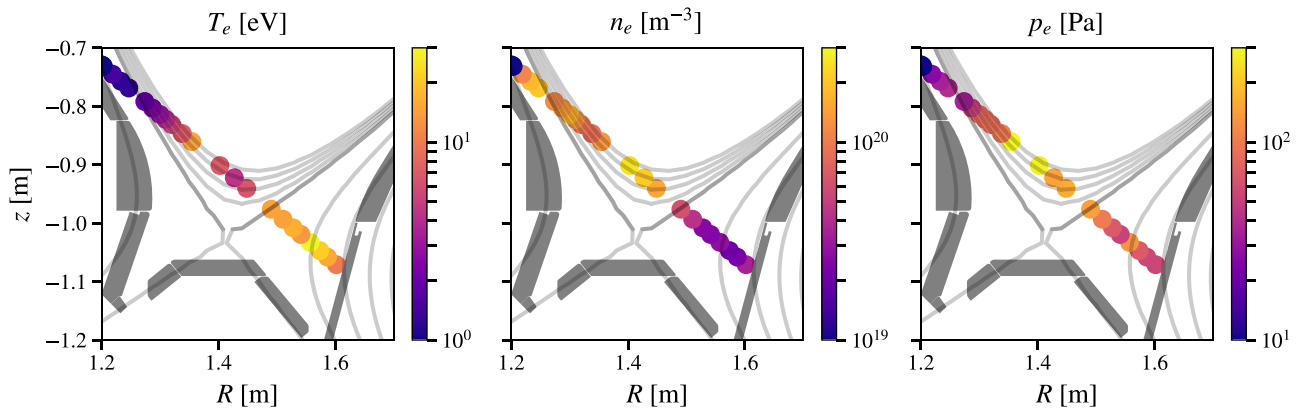


Figure 12. Measurements of T_e (a), n_e (b), and p_e (c) via DTS during a well-developed XPR using the plasma shape in figure 11(b).

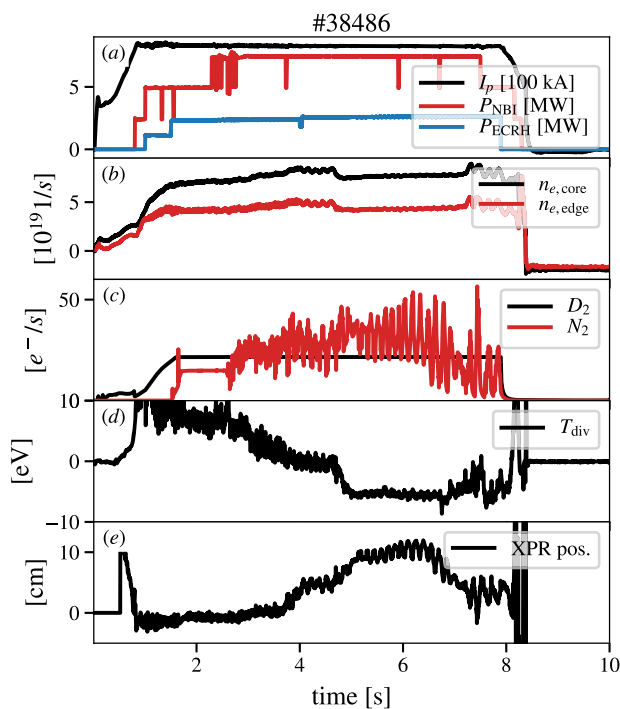


Figure 13. XPR-discharge using the shape in figure 11(a): (a) plasma current I_p (black), NBI P_{NBI} (red) and ECRH P_{ECRH} heating; (b) edge (red) and core (black) electron density; (c) deuterium (black) and nitrogen (red) seeding rates; (d) divertor temperature; (e) XPR position.

less constant during the whole discharge (note the linear scale in figure 14(c)), the mid-plane temperature decreases with the formation of the XPR. In figure 14(e) the evolution of the mid-plane and the X-point pressures (black) are compared and show a relatively good agreement throughout the whole discharge demonstrating that p_e is conserved on closed FSs. However, as stated before, there are large uncertainties in this comparison: the alignment is based on p_X calculated between 2 s and 4 s where the DTS is at the limit of its measurement range, the same applies to the measurements during the ELM suppression phase, furthermore the effect of a possible parallel pressure gradient in the equilibrium reconstruction, i.e. on the position of the X-point, it is not clear. On the other

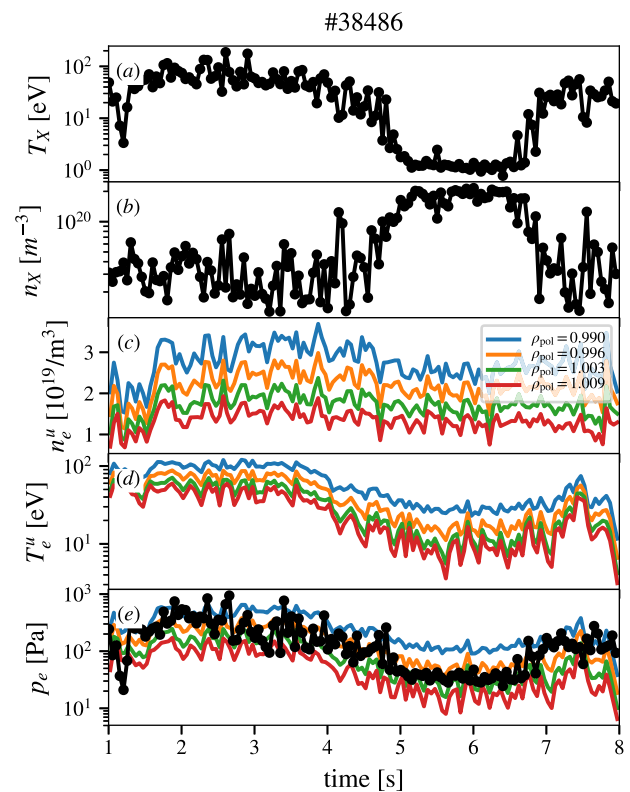


Figure 14. X-point T_e (a) and n_e (b) to the mid-plane T_e (c) and n_e (d) at different radial locations (different colors). The calculated electron pressures are compared in figure (e).

hand, while a certain drop of p_e might be possible within the uncertainties, it is highly unlikely that a pressure drop as in pronounced detachment could take place along closed field lines (figure 10(c)). Such a pressure gradient parallel to the field lines would be unstable from a magnetohydrodynamic point of view [41].

5. Conclusions and outlook

The newly installed DTS at AUG is shown to provide new insights into the divertor physics. Despite the closure of the

AUG divertor, a sweep method has been developed to collect 2D n_e and T_e measurements in the divertor volume while keeping the plasma constant in both L- and H-mode. In L-mode, this technique revealed a sharp transition from partial to pronounced detachment, similar to what was observed in H-mode in DIII-D [13], in which the interplay between outer and inner divertor seems to play a crucial role. Furthermore, during the detachment, a clear parallel electron pressure gradient starting close to the separatrix and extending to complete SOL could be confirmed via DTS. The H-mode discharges show a similar phenomenological behavior compared to the L-mode when going to detachment but further investigations are necessary to confirm or exclude the presence of a bifurcation when going to pronounced detachment. The 2D measurements highlighted the presence of a relatively high density, of the order of 10^{20} m^{-3} , in the PFR which is not present in L-mode providing an interesting case study for divertor modelling. Dedicated discharges have been performed to characterize the XPR. By moving the X-point almost on the divertor dome PFCs, the DTS can access the confined plasma just above the X-point. During a well-developed and stable XPR, local temperatures of about 1 eV, accompanied by densities on the order of 10^{20} m^{-3} , have been observed within the separatrix and next to the X-point. The comparison between the upstream and the X-point pressure shows that, within the uncertainties of the DTS and the equilibrium reconstruction, the electron pressure is largely conserved along the closed field lines. This is an exciting result which shows the possibility to have stable plasmas with temperature as low as ≈ 1 eV within the confined region.

The possibility to access to 2D n_e and T_e profiles of a large part of the divertor is a breakthrough for divertor studies at AUG. For example, the combination of the measurements shown in this work with the divertor spectroscopy will allow the assessment of the divertor neutral density and in turn of the plasma particle balance [42, 43]. Furthermore, it provides an extremely valuable benchmark and input for any modeling activity.

Acknowledgments

The authors would like to thank A. McLean for fruitful discussions and valuable input. This work has been carried out within the framework of the EUROfusion Consortium, funded by the European Union via the Euratom Research and Training Programme (Grant Agreement No. 101052200 — EUROfusion). Views and opinions expressed are however those of the author(s) only and do not necessarily reflect those of the European Union or the European Commission. Neither the European Union nor the European Commission can be held responsible for them.

ORCID iDs

M. Cavedon  <https://orcid.org/0000-0002-0013-9753>

D. Brida  <https://orcid.org/0000-0002-8647-7058>

M. Griener  <https://orcid.org/0000-0003-2953-536X>

S. Henderson  <https://orcid.org/0000-0002-8886-1256>

T. Nishizawa  <https://orcid.org/0000-0003-1804-2308>

T. Lunt  <https://orcid.org/0000-0002-7386-1456>

O. Pan  <https://orcid.org/0000-0003-3827-0674>

U. Stroth  <https://orcid.org/0000-0003-1104-2233>

References

- [1] Kurzan B., Lohs A., Sellmair G. and Sochor M. 2021 *J. Inst.* **16** C09012
- [2] Loarte A. et al 2007 *Nucl. Fusion* **47** S203–63
- [3] Federici G., Biel W., Gilbert M.R., Kemp R., Taylor N. and Wenninger R. 2017 *Nucl. Fusion* **57** 092002
- [4] Gruber O., Marinari E. and Vespignani A. 1995 *Phys. Rev. Lett.* **74** 4217–20
- [5] Loarte A. et al 1998 *Nucl. Fusion* **38** 331–71
- [6] Lipschultz B. et al 1995 *J. Nucl. Mater.* **220–222** 50–61
- [7] Petrie T.W. et al 1997 *Nucl. Fusion* **37** 321–38
- [8] Leonard A.W. 2018 *Plasma Phys. Control. Fusion* **60** 044001
- [9] Krasheninnikov S.I., Kukushkin A.S. and Pshenov A.A. 2016 *Phys. Plasmas* **23** 055602
- [10] Stangeby P.C. 2018 *Plasma Phys. Control. Fusion* **60** 044022
- [11] Röhr H., Steuer K.-H., Schramm G., Hirsch K. and Salzmann H. 1982 *Nucl. Fusion* **22** 1099–102
- [12] Carlstrom T.N., Hsieh C.L., Stockdale R., Nilson D.G. and Hill D.N. 1997 *Rev. Sci. Instrum.* **68** 1195–200
- [13] McLean A.G. et al 2015 *J. Nucl. Mater.* **463** 533–6
- [14] Bernert M. et al 2017 *Nucl. Mater. Energy* **12** 111–8
- [15] Potzel S., Wischmeier M., Bernert M., Dux R., Müller H.W. and Scarabosio A. 2013 *Nucl. Fusion* **54** 013001
- [16] Dunne M.G. 2013 Inter-ELM evolution of the edge current density profile on the ASDEX Upgrade tokamak *PhD Thesis* University College Cork
- [17] Kallenbach A. et al 2010 *Plasma Phys. Control. Fusion* **52** 055002
- [18] Potzel S. et al 2015 *J. Nucl. Mater.* **463** 541–5
- [19] Jaervinen A.E. et al 2018 *Phys. Rev. Lett.* **121** 075001
- [20] Kukushkin A.S. and Krasheninnikov S.I. 2019 *Plasma Phys. Control. Fusion* **61** 074001
- [21] Fischer R., Fuchs C.J., Kurzan B., Suttrop W. and Wolfrum E. 2010 *Fusion Sci. Technol.* **58** 675–84
- [22] Schneider P.A. 2012 Characterization and scaling of the tokamak edge transport barrier *PhD Thesis* (https://edoc.ub.uni-muenchen.de/14723/1/Schneider_Philip.pdf)
- [23] Davies S. et al 1997 *J. Nucl. Mater.* **241–243** 426–32
- [24] Loarte A., Monk R.D., Kukushkin A.S., Righi E., Campbell D.J., Conway G.D. and Maggi C.F. 1999 *Phys. Rev. Lett.* **83** 3657–60
- [25] Heinrich P. et al 2020 *Nucl. Fusion* **60** 076013
- [26] Fussmann G. et al 1984 *J. Nucl. Mater.* **128–129** 350–8
- [27] Stangeby P.C. 1995 *Plasma Phys. Control. Fusion* **37** 1031–7
- [28] Carlson A. and Weinlich M. 1998 *Contrib. Plasma Phys.* **38** 38–46
- [29] Février O., Theiler C., De Oliveira H., Labit B., Fedorczak N. and Baillod A. 2018 *Rev. Sci. Instrum.* **89** 053502
- [30] The JET Team 1995 *Plasma Phys. Control. Fusion* **37** A227–39
- [31] Lipschultz B., LaBombard B., Terry J.L., Boswell C. and Hutchinson I.H. 2007 *Fusion Sci. Technol.* **51** 369–89
- [32] Kallenbach A. et al 2015 *Nucl. Fusion* **55** 053026
- [33] Frassinetti L. et al 2016 *Nucl. Fusion* **57** 022004
- [34] Harrer G.F. et al 2018 *Nucl. Fusion* **58** 112001
- [35] Bernert M. et al 2020 *Nucl. Fusion* **61** 024001
- [36] Rognlien T.D. et al 2017 *Nucl. Mater. Energy* **12** 44–50

- [37] Xu G. *et al* 2020 *Nucl. Fusion* **60** 086001
- [38] Eldon D. *et al* 2019 *Nucl. Mater. Energy* **18** 285–90
- [39] Nakano T., Kubo H., Asakura N., Shimizu K., Kawashima H. and Higashijima S. 2009 *J. Nucl. Mater.* **390–391** 255–8
- [40] Reimold F., Wischmeier M., Bernert M., Potzel S., Kallenbach A., Müller H.W., Sieglin B. and Stroth U. 2015 *Nucl. Fusion* **55** 033004
- [41] Zohm H 2014 *Magnetohydrodynamic Stability of Tokamaks* (New York: Wiley)
- [42] Nishizawa T., Cavedon M., Reimold F., Dux R., Brida D. and Wu H. 2020 *Plasma Phys. Control. Fusion* **62** 085005
- [43] Verhaegh K. *et al* 2021 *Nucl. Mater. Energy* **26** 100922